PHYSICAL REVIEW B **76**, 214410 (2007)

Phase imaging of magnetic nanostructures using resonant soft x-ray holography

A. Scherz,[1,*] W. F. Schlotter,[1,2] K. Chen,[1,2] R. Rick,[1,2] J. Stöhr,[1] J. Lüning,[1] I. McNulty,[3,4] Ch. Günther,[3] F. Radu,[3]
W. Eberhardt,[3] O. Hellwig,[3,5] and S. Eisebitt[3]
[1]*SSRL, Stanford Synchrotron Radiation Laboratory, 2575 Sand Hill Road, Menlo Park, California 94025, USA*
[2]*Department of Applied Physics, 316 Via Pueblo Mall, Stanford University, Stanford, California 94035-4090, USA*
[3]*BESSY m.b.H., Albert-Einstein-Strasse 15, 12489 Berlin, Germany*
[4]*Argonne National Laboratory, 9700 S. Cass Avenue, Argonne, Illinois 60439, USA*
[5]*San Jose Research Center, Hitachi Global Storage Technologies, 3403 Yerba Buena Road, San Jose, California 95135, USA*
(Received 17 October 2007; published 17 December 2007)

We demonstrate phase imaging by means of resonant soft x-ray holography. Our holographic phase-contrast method utilizes the strong energy-dependence of the refractive index at a characteristic x-ray absorption resonance. The general concept is shown by using a Co/Pd multilayer sample which exhibits random nanosized magnetic domains. By tuning below the Co *L*-edge resonance, our quantitative and spectroscopic phase method allows high-contrast imaging of nanoscale electronic and magnetic order while increasing the probing depth and decreasing the radiation dose by an order of magnitude. The complex refractive index is quantitatively obtained through the interference between resonant and nonresonant scattering.

DOI: 10.1103/PhysRevB.76.214410 PACS number(s): 78.70.Ck, 42.30.Wb, 42.40.Kw, 78.70.Dm

Over the last decade, phase contrast imaging in x-ray microscopy has been employed to enhance image contrast in weakly absorbing specimens such as biological or polymer samples.[1–6] Phase sensitivity can be realized in differential interference (phase gradient) contrast and Zernike phase contrast methods. These real space techniques require special optical elements for rendering phase modulations imposed on the wave field by the object. At present, all real space x-ray imaging techniques are limited to a spatial resolution of about 15 nm by x-ray optics.[7] In contrast, lensless imaging methods based on coherent x-ray scattering are only limited by the wavelength and not by optics, and are thus capable of achieving wavelength limited resolution. This approach is based on retrieving a real space image from a reciprocal space interference or "speckle" pattern of the sample. Image reconstruction can be performed either directly from the speckle pattern by phase retrieval algorithms[8–11] or by experimentally encoding the speckle pattern by a reference wave in the so-called Fourier transform holography (FTH), where the real space image is obtained by simple Fourier transform inversion.[12–14]

Here, we demonstrate phase imaging using resonant soft x-ray holography. The technique is based on tuning the photon energy to an element-specific core electron binding energy of the sample, and utilizing the fact that the real part (phase) and the imaginary part (absorption) of the complex refractive index $n(\omega)$ have resonant maxima at slightly different energies in the vicinity of an absorption resonance, thus providing enhanced image contrast. A phase-dominated x-ray hologram is recorded by tuning the photon energy just below the absorption resonance (peak). In contrast, an absorption-dominated x-ray hologram is recorded at slightly higher energy by tuning to the absorption peak itself. Both methods rely on the reconstruction of the real space sample transmittance from the Fraunhofer diffraction pattern by using either the real or imaginary part of the Fourier transform. Phase imaging offers an important advantage over absorption imaging. It decreases electronic excitations which may result in radiation damage while utilizing the resonant maximum in the phase to enhance sensitivity to ultrathin structures and buried interfaces with nanoscale resolution. The utilized resonant aspect of x-ray scattering furthermore combines structural with electronic and magnetic information, rendering this approach applicable to many research fields such as magnetism and correlated materials as well as polymeric or macromolecular systems.

We demonstrate the general concept by direct comparison of holographic phase and absorption imaging of nanoscale magnetic domains in a Co/Pd multilayer tuning the x-ray energy across the Co *L*-edge resonance. We show through a quantitative analysis how the phase and absorption information of the object is encoded in the symmetry dependent interference terms between charge and magnetic scattering. The symmetry properties provide more information about the object texture which in turn can aid image reconstruction from non-holographic speckle patterns. We also show that phase imaging lessens the impact of beam stops. Finally, the radiation dose using resonant phase imaging is shown to be effectively ten times smaller for comparable image contrast than absorption imaging. The phase method is fully compatible with multiple reference FTH, which improves image quality by simultaneously recording multiple images.[15] Therefore, our results also suggest how to mitigate sample perturbations or damage in resonant ultrafast single-shot imaging with x-ray lasers.

Experiments were performed on the soft x-ray beam line 5-2 at the Stanford Synchrotron Radiation Laboratory using the experimental arrangement illustrated in Fig. 1. Circularly polarized x rays from an undulator source were energy filtered by a spherical grating monochromator. The photon energy was tuned to the Co L_3 edge ($\lambda = 1.59$ nm) with an energy resolution $E/\Delta E \approx 4000$, yielding a longitudinal coherence length of $\xi_l = 6.4$ μm. The beam was spatially filtered resulting in a transverse coherence length of $\xi_t > 5$ μm in the sample plane. The coherent small angle scattering pattern of the transmitted beam was recorded with an

©2007 The American Physical Society

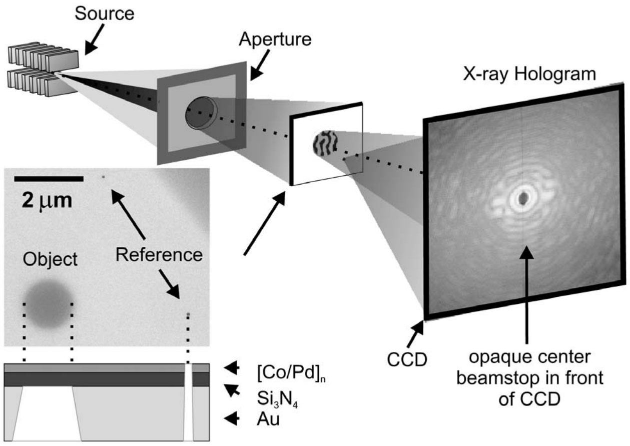

FIG. 1. Experimental setup for inline holography with soft x-ray synchrotron radiation from a variable polarization undulator and spherical grating monochromator. The source is made spatially coherent by an aperture. The coherent beam illuminates the holographic mask fabricated by FIB milling (inset: SEM image). The far-field diffraction pattern is recorded with a CCD. A beam stop is used to eliminate the direct beam.

in-vacuum backside-illuminated charge-coupled device (CCD) camera with 1300×1340 pixels of 20 μm in size. The distance r from the sample to the CCD was $r=135$ mm, corresponding to a field of view of 6×6 μm^2. Part of the experiments were also performed on the UE52-SGM beam line at BESSY (setup described in Ref. 16).

The magnetic $[\text{Co (2.5 Å)}/\text{Pd (9 Å)}]_{125}$ multilayer was sputter deposited on the front side of a 125×75 μm^2 Si$_3$N$_4$ membrane. This sample has a higher perpendicular magnetic anisotropy, fewer closure domains at the surface, and a higher transmission than previously investigated Co/Pt samples.[14,16] A 1 μm thick Au film, which is effectively opaque to soft x rays, was sputter deposited onto the back side of the membrane. The holographic structure was patterned into the Au film using focused ion beam (FIB) milling.[14] That way, an object aperture of 1.4 μm diameter was cut into the Au layer, stopping at the Si$_3$N$_4$ membrane. A scanning electron microscopy (SEM) image of the front side of the holographic mask is shown in Fig. 1. The object aperture is visible through the membrane. Two 90 nm sized reference holes are also visible. Both penetrate the entire structure 4 μm away from the object center. The easy magnetization direction of the multilayer was along the surface normal, and a magnetic worm domain pattern was created by demagnetization of the sample. The x-ray magnetic circular dichroism effect (XMCD) in transmission was used for magnetic contrast.

The transmittance of a thin sample at wavelength λ depends on the index of refraction $n=1-\delta+i\beta$,[17] circular polarization $\alpha=\pm1$, and the sample thickness d according to

$$T_\alpha(\xi,\eta)=\exp\left\{i\frac{2\pi}{\lambda}\int_0^d[n_\alpha(\xi,\eta,\zeta)-1]d\zeta\right\}. \qquad (1)$$

In the limit of weak contrast, i.e., $d\sim\lambda$, Eq. (1) simplifies to, $T_\alpha(\xi,\eta)\cong1-i\phi_\alpha(\xi,\eta)-\mu_\alpha(\xi,\eta)$, since in the soft x-ray range the dispersive and absorptive parts are small, $\delta,\beta\simeq10^{-3}$. The absorbing $\mu=(2\pi d/\lambda)\beta$ and the phase-shifting sample properties $\phi=(2\pi d/\lambda)\delta$ form the diffraction pattern and are characterized by the complex transmittance $T(\xi,\eta)$. Note that the real part δ of the refractive index generates the imaginary phase component ϕ of $T(\xi,\eta)$. In the Fraunhofer regime, the diffraction pattern reduces to a Fourier transform of the autocorrelation, $\mathcal{T}(x,y)=\int\int T(\xi,\eta)T^*(\xi-x,\eta-y)d\eta d\xi$, of the exit wave, i.e., the electric field distribution in the (x,y) plane directly behind the object. Because of the linearity of the Fourier transform, an absorption and phase reconstruction of the sample transmittance is simultaneously obtained from the respective real and imaginary parts of $\mathcal{T}$.

With x rays, we utilize the highly energy-dependent index of refraction in the vicinity of an absorption resonance (see Fig. 4) to select between phase and absorption imagings. Holograms where the image contrast primarily results from differences in either the absorption or the phase are shown in Fig. 2. The phase hologram in Fig. 2(a) was recorded by tuning the photon energy to 776.5 eV, or 1 eV below the absorption threshold, where the absorptive part β is strongly reduced. For the absorption hologram in Fig. 2(b), the photon energy was tuned to maximum absorption at 778.3 eV, where the dispersive part δ vanishes. Both patterns (a) and (b) were recorded with right circularly polarized x rays. Hence, by changing the photon energy by a few eV, real and imaginary parts of the complex transmittance can be probed separately. In total, $N=8\times10^8$ photons were accumulated in each hologram with a photon flux of $\sim4\times10^6$ photons/(s μm^2) impinging the sample. For the phase hologram, the 225 s accumulation time was 6.5 times shorter due to the higher transmission of the sample. In fact, at the energy of maximum absorption, 778.3 eV, the $1/e$ x-ray absorption length $1/\mu=\ln(I_0/I)d$ becomes as short as 17 nm but increases by a factor of 30 with 35% of the optimum absorption contrast at the energy of the phase hologram, 776.5 eV. Since the scattered intensity is proportional to the scattering contrast, the radiation dose is effectively ten times smaller for comparable image quality.

The prominent features in the x-ray holograms have been described in detail elsewhere.[14] The circular fringe pattern with the distinct magnetic speckles originates from the object. The high spatial frequency modulations in the pattern, resolved in the magnifications (c) and (e) of the center areas in Figs. 2(a) and 2(b), are caused by the object-reference interference. The phase and absorption information of the domain structure is encoded in the interference of the resonant magnetic scattering with the nonresonant charge scattering. The corresponding far-field intensities are therefore remarkably different depending on the resonant contrast mechanism. By taking the difference between holograms recorded with left and right circularly polarized lights in Figs. 2(d) and 2(f), the charge-magnetic interference remains.[18] The charge-magnetic interference reveals an odd centrosymmetry utilizing (d) the resonant phase contrast at 776.5 eV and an even centrosymmetry having (f) resonant absorption contrast at 778.3 eV. These symmetries are expected as they

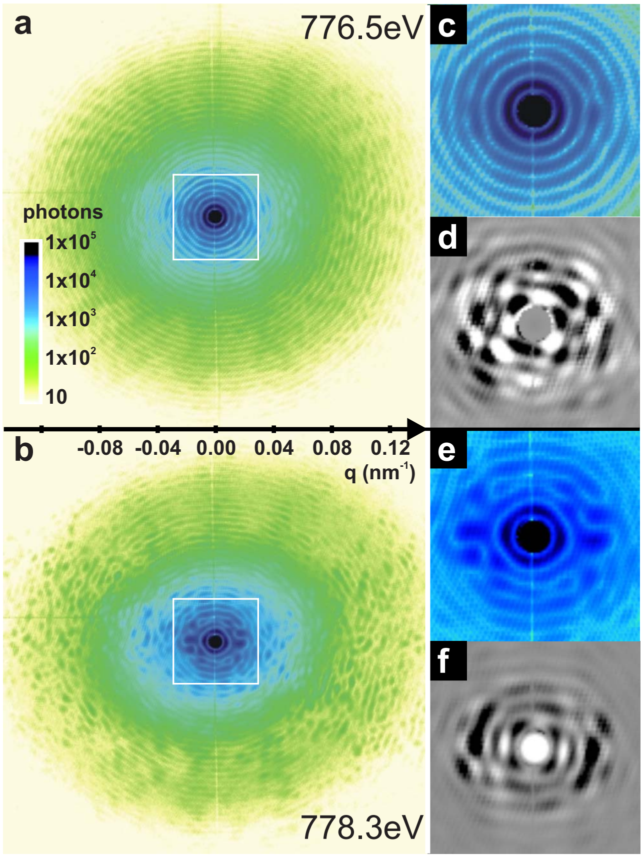

FIG. 2. (Color online) (a) Phase and (b) absorption holograms, recorded with right circularly polarized x rays at 776.5 and 778.3eV, respectively. (c) and (e) are magnifications of the centers of the phase and the absorption holograms (a) and (b). The photon counts are shown on a logarithmic scale. (d) and (f) show the difference between holograms recorded with left and right circularly polarized x rays of the center area at respective photon energies. The beam stop was replaced by an Airy disk to a momentum transfer of $q=0.002\ \text{nm}^{-1}$.

ensure the reconstruction of the absorption and phase image in the respective real and imaginary parts of the autocorrelation $\mathcal{T}$.

In Fig. 3, the symmetry properties of the complex autocorrelation $\mathcal{T}$ are demonstrated for right circularly polarized x rays at the rising L_3 edge where both μ and ϕ contribute having opposite signs. $\mathcal{T}$ contains the self-correlations of the object and the reference in the center and has the object-reference convolution $T_{\text{ref}}^{(-)}$ (upside-down image) and cross correlation T_{ref}^{*} (complex conjugate image) opposed to each other. The real part of $\mathcal{T}$ is thus even centrosymmetric, while the imaginary part is odd centrosymmetric. This is analog to the symmetry properties of the charge-magnetic interference. By conserving the symmetry, the Fourier transformation of the noncomplex diffraction pattern reassembles the absorption and phase images in the real and imaginary part of $\mathcal{T}$, accordingly. Phase or absorption imaging thus requires appropriate determination of the center of symmetry, i.e., $q=0$; otherwise possible shifts in the diffraction pattern cause cross-talk between the real and imaginary parts in the autocorrelation.

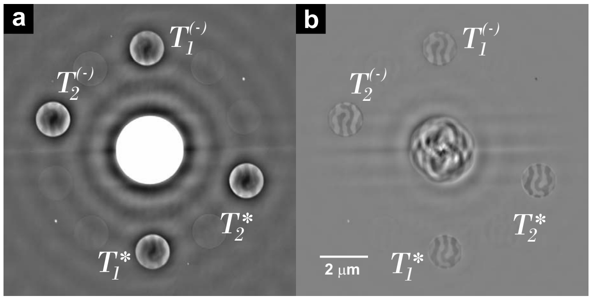

FIG. 3. (a) real part and (b) imaginary part of the autocorrelation as obtained at 777.7 eV with right circularly polarized x rays. The center in the real part is saturated due to limited gray scale range. Object-reference convolutions and cross correlations are indicated.

Typically, due to the limited dynamic range of CCDs, the presence of the direct beam on the detector impedes the high-q information which determines the real space resolution. If beam stops are used to eliminate the central beam, the quality of the image reconstruction depends on the appropriate replacement of the missing low-q part.[8] Phase imaging can partly overcome these problems, since the center area is governed by the real absorptive part in the transmittance, which

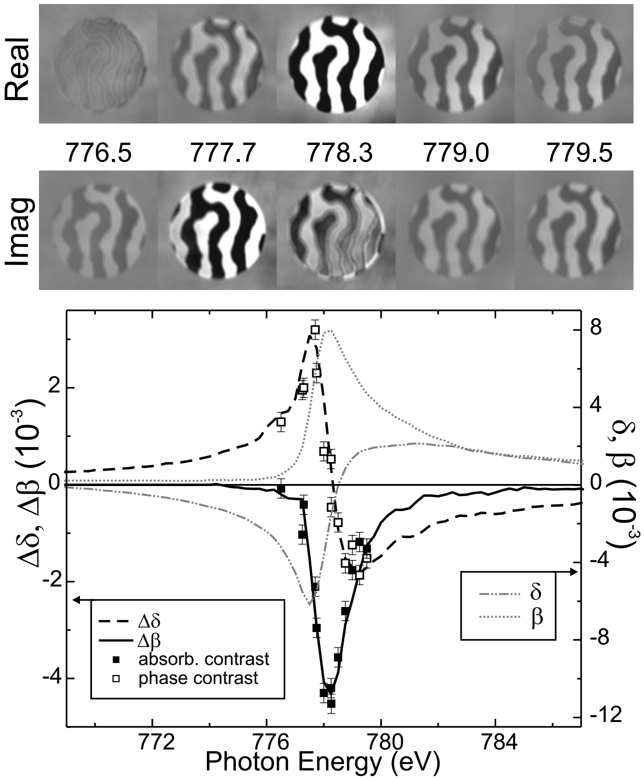

FIG. 4. Top: real (top row) and imaginary (bottom row) parts of the complex real space object image obtained from the holographic difference between left and right circularly polarized x rays as a function of photon energy across the L_3 edge. Bottom: photon energy dependence of the optical constants δ (dashed-dotted) and β (dotted) and the differences $\Delta\delta$ (dashed) and $\Delta\beta$ (solid) of the two polarizations. Spectra are provided by Kortright *et al.* (Ref. 19). Data points are taken from the image contrast.

is $T_\alpha = 1 - \mu(\xi, \eta) \approx 1$. In our experiment, a round 200 μm beam stop held by a wire of 14 μm in diameter was used to block the direct beam. The hidden low-q information was replaced in first approximation by fitting an Airy function up to $q = 0.002$ nm^{-1}, corresponding to the diffraction from the object aperture, as shown in Fig. 2. This even centrosymmetric replacement leads to finite ringing effects in the autocorrelation, whereby the absorption image is much more affected than the nearly undisturbed phase image.

The direct relation between images recorded by absorption and phase contrast is demonstrated in Fig. 4. The reconstructed images were obtained at characteristic photon energies across the L_3 absorption edge from the holographic differences $\Delta T^{(-)} = T^{(-)}_{+1} - T^{(-)}_{-1}$ of right and left circular polarized lights ($\alpha = \pm 1$). The magnetic absorption contrast (top row) varies as expected being maximal at the absorption resonance energy. The magnetic phase contrast (bottom row) first exhibits the inverted contrast before the absorption edge and then reverses its sign with an overall dispersive-like envelope, a clear indication of phase contrast sensitivity. Please note that 778.3 eV is slightly above the L_3 edge and thus, a small and reverted phase image is remaining. The complex image contrast can be further quantitatively analyzed. The contrast in the images is due to the domain pattern in the magnetic Co layers of constant total thickness $d = 31.3$ nm. In principle, the optical constants can then be absolutely determined from the ratio of the two autocorrelations for $\alpha = \pm 1$ according to Eq. (1). Here, limited by missing low-q information, the spin-dependent index of refraction for Co has been relatively extracted from the black and white contrasts corresponding to up and down oriented magnetic domains and plotted against the photon energy. The data have then been rescaled by a single scaling factor to match the Co optical constants which had previously been determined for a Co/Pt multilayer from x-ray absorption and XMCD spectra in Ref. 19.

Finally, by recording both the phase and the absorption dominated holograms, more information about the object texture is provided, as revealed in Fig. 2. This can be used to aid recovery of its image in nonholographic diffraction experiments with a modified phase retrieval algorithm. This type of experiment can only be performed with resonantly tuned x rays, where the photon energy or wavelength is varied by a few permille only around specifiable and well-separated absorption edges.

In conclusion, we have demonstrated phase imaging with resonantly tuned soft x rays by means of Fourier transform holography. Our high contrast method provides nanoscale images of the electronic and magnetic structures by utilizing a resonance in the phase and avoiding an adjacent resonance in absorption. As such the technique should be of great value for radiation sensitive samples, such as biological specimens or polymers. In such systems, phase contrast just below the K-absorption edges of important elements such as carbon, nitrogen, oxygen, or sulfur will reduce radiation damage and enhance the sensitivity to buried ultrathin interfaces.[20] We also propose that the combination of phase and absorption information available in the diffraction patterns can improve current phase retrieval algorithms in coherent scattering. Finally, we suggest that phase imaging in combination with multiple reference FTH provides an effective path to alleviate sample perturbations in resonant ultrafast single-shot imaging with x-ray lasers.

The authors are grateful to J. Kortright for providing the Co optical constants. Portions of this research were carried out at the Stanford Synchrotron Radiation Laboratory (SSRL), a national user facility. SSRL and the research of the SSRL authors are funded by the U.S. Department of Energy, Office of Basic Energy Sciences (DOE-BES). I.M. acknowledges support by DOE-BES and the European Union Marie Curie Foundation under contract No. MTKD-CT-2004-0003178.

---

*Corresponding author. scherz@slac.stanford.edu

[1] T. J. Davis, D. Gao, T. E. Gureyev, A. W. Stevenson, and S. W. Wilkins, Nature (London) **373**, 595 (1995).

[2] G. Schmahl, D. Rudolph, P. Guttmann, G. Schneider, J. Thieme, and B. Niemann, Rev. Sci. Instrum. **66**, 1282 (1995).

[3] S. C. Mayo, T. J. Davis, T. E. Gureyev, P. R. Miller, D. Paganin, A. Pogany, A. W. Stevenson, and S. W. Wilkins, Opt. Express **11**, 2289 (2003).

[4] K. A. Nugent, A. G. Peele, H. N. Chapman, and A. P. Mancuso, Phys. Rev. Lett. **91**, 203902 (2003).

[5] F. Pfeiffer, T. Weitkamp, O. Bunk, and C. David, Nat. Mater. **2**, 258 (2006).

[6] C. Chang, A. Sakdinawat, P. Fischer, E. Anderson, and D. Attwood, Opt. Lett. **31**, 1564 (2006).

[7] W. Chao, B. D. Harteneck, J. A. Liddle, E. H. Anderson, and D. T. Attwood, Nature (London) **435**, 1210 (2005).

[8] J. Miao, P. Charalambous, J. Kirz, and D. Sayre, Nature (London) **400**, 342 (1999).

[9] H. N. Chapman, *et al.*, J. Opt. Soc. Am. A **23**, 1179 (2006).

[10] I. K. Robinson, I. A. Vartanyants, G. J. Williams, M. A. Pfeifer, and J. A. Pitney, Phys. Rev. Lett. **87**, 195505 (2001).

[11] D. Shapiro, *et al.*, Proc. Natl. Acad. Sci. U.S.A. **102**, 15343 (2005).

[12] G. W. Stroke and D. Falconer, Phys. Lett. **13**, 317 (1964).

[13] I. McNulty, J. Kirz, C. Jacobsen, E. H. Anderson, M. R. Howells, and D. P. Kern, Science **256**, 1009 (1992).

[14] S. Eisebitt, J. Lüning, W. F. Schlotter, M. Lörgen, O. Hellwig, W. Eberhardt, and J. Stöhr, Nature (London) **432**, 885 (2004).

[15] W. F. Schlotter, *et al.*, Appl. Phys. Lett. **89**, 163112 (2006).

[16] O. Hellwig, S. Eisebitt, W. Eberhardt, W. F. Schlotter, J. Lüning, and J. Stöhr, J. Appl. Phys. **99**, 08H307 (2006).

[17] The dimensionless optical constants $\delta(\omega)$ and $\beta(\omega)$ are related to the scattering factors $f_1(\omega) = Z + f'(\omega)$ and $f_2(\omega) = f''(\omega)$ in units of number of electrons according to $\delta(\omega) = \frac{r_0 \lambda^2}{2\pi} \rho f_1(\omega)$, and $\beta(\omega) = \frac{r_0 \lambda^2}{2\pi} \rho f_2(\omega)$, where Z is the number of atomic electrons, r_0 is the classical electron radius, λ is the x-ray wavelength, and

ρ is the atomic number density.

[18] S. Eisebitt, M. Lörgen, W. Eberhardt, J. Lüning, J. Stöhr, C. T. Rettner, O. Hellwig, E. E. Fullerton, and G. Denbeaux, Phys. Rev. B **68**, 104419 (2003).

[19] J. B. Kortright, S.-K. Kim, G. P. Denbeaux, G. Zeltzer, K. Takano, and E. E. Fullerton, Phys. Rev. B **64**, 092401 (2001).

[20] R. A. London, M. D. Rosen, and J. E. Trebes, Appl. Opt. **28**, 3397 (1989).